Exploring Spin Dynamics in Diatomic Co_2 Catalysts on Graphyne for Enhanced CO Electroreduction

Shuang-Te Zhao, [#] *Wei Zhang,* [#] *Xue-long Zhang, Cun-biao Lin, Wen-xian Chen, Gui-lin Zhuang**

H-PSI Computational Chemistry Lab, Institute of Industrial Catalysis, State Key Laboratory Breeding Base of Green-Chemical Synthesis Technology, College of Chemical Engineering, Zhejiang University of Technology, Hangzhou 310032, P.R. China

[#] These authors contributed equally to this work,

* Corresponding Author, Email: glzhuang@zjut.edu.cn

Abstract

Investigating spin dynamics in electrocatalysis is crucial for the rational design of paramagnetically heterogeneous catalysts. Utilizing spin-polarized density functional theory (DFT) calculation, herein, we identify spin dynamic of diatomic Co_2-supported γ-graphyne (Co_2-GY) catalysts during the process of CO electroreduction (eCORR), focusing on the effect of the applied potential and acidy on spin dynamic and catalytic performance. Specially, the obtained Co_2-GY shown a new efficient C_2 pathway of CH_2* + CHO* coupling mechanism, resulting in the optimal CH_3CH_2OH product with ΔG of 0.50 eV and the selectivity of 99.99% under alkaline condition. Under acidic media, Co_2-GY exhibited the optimal C_1 product (CH_3OH) with ΔG of 0.27 eV and the selectivity of 99.99%. During CO electroreduction, the reaction environment (pH and applied potential) influences spin dynamics in catalyst-reactant systems, affecting the spin transition of diatomic Co_2 active sites among four magnetic states: ferromagnetic, antiferromagnetic, paramagnetic, and diamagnetic. These finding will be helpful for rational design of transition-metal heterogeneous catalysts.

Keywords: Spin Dynamic; Dual Metal-Atom Catalyst; CO electroreduction; Applied Potential

1. Introduction

The latest five years have witnessed that carbon neutrality, balancing between emitting carbon and absorbing carbon from the atmosphere, is spurring a large research effort to develop new photocatalysts/electrocatalyst for the conversion from CO_2 to high value-added chemicals (e.g., CH_4,[1-4] CH_3OH,[5, 6] CH_3CH_3,[7-9] CH_3CH_2OH,[10-12] HCOOH[13, 14] et al.). However, the complexity of the proton-coupled electron transfer (PCET) process in CO_2 reduction, influenced by various factors including catalyst properties and reaction conditions, has limited the selectivity of these technologies for specific products, hindering their commercialization. Fortunately, the exceptionally high conversation rates (>99%) from CO_2 to CO was developed at commercially viable levels because of relatively simple two-step PCET process.[15, 16] Therefore, CO, as a pivotal intermediate, opens the possibility of breaking down CO_2 reduction into two distinct stages: CO_2 to CO conversion and CO reduction. Therefore, the exploration of high-selectivity catalysts for CO reduction (CORR) holds promise for advancing CO_2 reduction technologies (CO_2RR).

Electronically, unlike orbital property, which relates to the spatial distribution of electrons, spin is an intrinsic property of electrons and is mainly responsible for the magnetic behavior of atoms. Heterogeneous catalytical property, in the presence of non-quenched magnetic moments of active sites and corresponding interactions, is influenced by spin dynamic (e.g. magnetic exchange) as well as the orbital properties both geometrically and electronically. The effect of spin dynamic on chemistry (e.g. radical reaction) [17-25] and biology (e.g. magnetoreception of bird) [26] was realized half a century ago. In recent years, much effort has been paid to the enhancing role of spin dynamic induced by magnetic field on catalytic properties, such as oxygen evolution reaction (OER), oxygen reduction reaction (ORR), nitrogen reduction reaction (NRR). For instance, Shen et al.[27] found effective magnetic field regulation of the radical pair spin states during electron-transfer process for the enhanced properties of CO_2 electroreduction. Sun et al.[28] revealed the transition from ferrous to ferromagnetic behavior in NiFe-LDHS, impacting OER performance, especially with Cu^{2+} influence. Yu et al.[29] demonstrated the significance of magnetic coupling in $CoMN_6$-gra(OH) for

enhancing ORR performance. Dang et al. [30] improved NRR catalytic activity by controlling the electron spin moment of Mo in MoS_2 via doped metal atoms. While electronic properties related to orbital degrees of freedom, such as metal-support interaction and d-band center theory, have been extensively studied, the spin dynamics during catalytic processes, especially in the context of the interaction between reaction species and active sites, remained unclear both experimentally and theoretically.

Herein, we utilized spin polarization DFT calculation to investigate spin dynamic behaviors of magnetic Co_2 supported on γ-graphyne (Co_2-GY) dual metal-atom catalyst (DMAC) during eCORR process, focusing on the electrochemical environment and spin dynamic on the activity and selectivity. Specially, rection condition, e.g. solvent acid and applied potential, were taken into account under constant-potential implicit solvent model, and different magnetic states of Co_2-GY were considered. Co_2-GY displays intriguing spin dynamics with magnetic exchange between two Co ions, and thereby features a novel and efficient C-C coupling mechanism. It is found that Co_2-GY shown the outstanding catalytic activity and selectivity for CH_3CH_2OH.

2. Computational Details

Spin-polarized density functional theory (DFT) calculations were carried out utilizing the Vienna Ab initio simulation package (VASP 6.3.1).[31] The Perdew-Burke-Ernzerhof (PBE) functional within the generalized gradient approximation (GGA) was used to describe the exchange-correlation interaction in Kohn-shame equation.[32, 33] The projector-augmented wave $(PAW)^3$-based pseudopotential, featuring the greater computational efficiency and high accuracy, was utilized to describe the interaction between ions and electrons.[34, 35] The cutoff energy of 400 eV was used to expand plane wave function to describe valence electrons. For all calculations, the convergence thresholds for energy and force were set to 10^{-5} eV and 0.05 eV/Å, respectively. k-points sampling of 3×3×1 following Monkhorst-Pack strategy was used for structural optimization, while a comparatively denser k-points grid of 9×9×1 was used for the electronic structure and magnetic-property calculations.[36] A vacuum layer of 15 Å was used to prevent the interaction between periodic images. The DFT-D3 method of Grimme was used to correct the vdW interactions.[37, 38] The VASPKIT code was used

for postprocessing of the VASP computational data.[39] To confirm the magnetic state, Dudarev's formulation[40] with a Hubbard model (U_{eff} = 5.25 eV for Co, 5.16 for Fe and 4.967 for Ni)[41] was utilized to include strong correlation effects of 3*d* electrons. The effective Hubbard (U_{eff}) values of Co and Fe were calculated utilizing linear response method[42]. To validate PBE+U results, we utilized the OPBE functional, derived from OPTX exchange functional[43], known for its computational reliability and efficiency in describing the electronic structure of transition metals,[44] in the self-consistent field (SCF) calculation. More computational details were given in the Supporting Information.

The Gibbs free energy (ΔG) was calculated as followed:[45]

$$\Delta G = \Delta E_{DFT} + \Delta ZPE - T\Delta S + \Delta G_{pH} + \Delta G_U \quad \text{Eq (1)}$$

where ΔE_{DFT} is the system energy from DFT calculation. ΔZPE represents the zero-point energy by frequency calculation. Temperature T is equaled to 298.15 K. ΔS is entropy. The ΔZPE and ΔS of steady intermediates of C_1/C_2 reaction pathways were listed in **Table S20-S21**. The ΔG_{pH} and ΔG_U are defined as follow:

$$G_U = -neU \quad \text{Eq (2)}$$

where n is the transferred electron number. U is neglected in calculation.

$$G_{pH} = -k_B T \ln(H^+) = pH \times k_B T \ln 10 \quad \text{Eq (3)}$$

where k_B is the Boltzmann constant. pH is typically set as zero in all calculations.

The selectivity of C_2/CORR was estimated according to the Boltzmann distribution:

$$f_{C2/CORR} = 1/[1+\exp(\delta G/k_B T)] \quad \text{Eq (4)}$$

where δG is the difference in free-energy change between two competitive reactions, k_B is the Boltzmann constant, and T is the temperature.

The double-reference method was employed to simulate the electrochemical metal/solution interface and to evaluate the effects of solvation and the applied potential on the whole catalytic reaction.[46, 47] Specially, the solvent environment was described by implicit solvation model utilizing the VASPsol,[48, 49] and the relative permittivity of 80 was set to model the aqueous electrolyte. To mimic the compensating charge, the linearized Poisson−Boltzmann model was applied with a Debye length of 3.0 Å. To clarify the reaction mechanism under different electrode potentials, we added the excess

charge of the unit cell (Δn) from −2.0 e to +2.0 e with step size of 1e. The optimal magnetic state under the constant-potential model is obtained by the combination of the potential correlation curves of each intermediate under different magnetic states and pH corrected energy.

The electric potential of the slab referenced to the SHE is formulated in Eq 5.

$$U_q \text{ (V/SHE)} = \text{-4.6 V} - \Phi_q/e \qquad \text{Eq (5)}$$

where $-\Phi_q$ is the work function of the charged system. −4.6 V is the absolute electrode potential of the SHE benchmarked in VASPsol.

The potential-dependent energy of the system (E) is defined in Eq 6.

$$E = E_{DFT} - \Delta n(V_{sol} - \Phi_q/e) \qquad \text{Eq (6)}$$

where E_{DFT} is the DFT-calculated energy, V_{sol} is the electrostatic potential of the bulk electrolyte.

The E−U_q points follow a quadratic function as

$$E(U_q) = \text{-}1/2C(U_q - U_0)^2 + E_0 \qquad \text{Eq (7)}$$

where U_0, C, and E_0 are the fitted values of the potential of zero charge (PZC), capacitance of the corresponding system, and the energy of the system at the PZC, respectively.

3. Results and Discussion

3.1 Geometry and Magnetic Configuration

Firstly, the optimized γ-graphyne (GY) with lattice constants of 13.79 Å, compatible with previously reported results, was presented in **Figure 1a**. Structurally, the average C-C bond attains the lengths of 1.22 Å for sp-sp carbons, 1.41 Å for sp-sp^2 carbons and 1.41 Å for sp^2-sp^2 carbon in two neighboring C_{12} rings, respectively (see **Figure S1** and **Table S1**-**S2**). Transition metals, especially for VIII group metals, usually exhibits good catalytic activity for heterogeneous catalysis. Thus, three VIII group transition metals, consisting of Fe, Co and Ni, were selected as theoretical active site and load on GY by the d-π types coordination bonds of M and acetylene, resulting in three types of DMACs (label as M_2-GY) as shown in **Figure 1b**. Structurally, two adjacent metal ions in γ-graphyne feature the distance of 3.85 Å by an acetylene bond.

Electronically, two adjacent paramagnetic (PM) metals feature two types of magnetic

exchange, containing spin-parallel ferromagnetic (FM) state and spin-antiparallel anti-ferromagnetic (AFM) state. Thus, magnetic ground states of M_2-GY were firstly identified. As is well-known, Fe, Co and Ni ions experimentally feature two valence states (+2 and +3), leading to the different d-block electron conformations (Fe: $3d^5$, $3d^6$; Co: $3d^6$, $3d^7$; Ni: $3d^7$, $3d^8$). To identify electronic configuration of FM and AFM ground states of DMACs, the initial structures with possible unpaired electron number were fully relaxed (see **Figure S2-S3** and **Table S3)**. Clearly, it is revealed that (1) Each Fe of Fe_2-GY both FM and AFM states feature +2 valence with triplet. (2) Each Co of Co_2-GY both FM and AFM attains features +2 with doublet. (3) Each Ni atoms of Ni_2-GY for FM and AFM states feature closed-shell electronic configuration with +2 valence. Subsequently, magnetic ground state of M_2-GYs was further identified. However, accurately determining these states was challenging due to the self-interaction error associated with the pure PBE functional. Thus, through the contrast calculations (PBE, OPBE and PBE+U), we validated that Fe_2/Co_2-GY thermodynamically features weak ferromagnetic property (see **Table S4**). Such magnetic properties are mainly contributed by ferromagnetic exchange between two paramagnetic Fe/Co metals (see **Table S3)**. The partial density of states (PDOS) of d orbitals in Fe/Co on ground states Fe_2/Co_2-GY (see **Figure 1d** and **Figure S3)** shown obvious spin polarization between the PDOS of spin-up and spin-down (see **Table S3**). The spin arrangements in five d orbitals of Fe/Co on ground-states FM and AFM Fe_2/Co_2-GY are fascinating. The optimized structures of ground states FM and AFM Fe_2/Co_2-GY were exhibited in **Figure S4**. Take Co_2-GY as an example. From **Figure S4**, the Co and GY were in a plane, as well as each Co is coordinated by three C≡C bonds of GY via the π-type electron pairs, resulting in the planar triangular coordination fields with D_{3h} symmetry. According to coordination field theory, the splitting of *d* orbitals is depicted in **Figure 1e-1f** for FM and AFM Co_2-GY. The double degenerate d_{xy} and d_{x2-y2} orbitals was singularly occupied by unpair electron, which propagates with the adjacent Co^{2+} ion via the supper-exchange interaction of C≡C. Similarly, the magnetic configurations of ground states FM and AFM Fe_2-GY were traced in **Figure S5**.

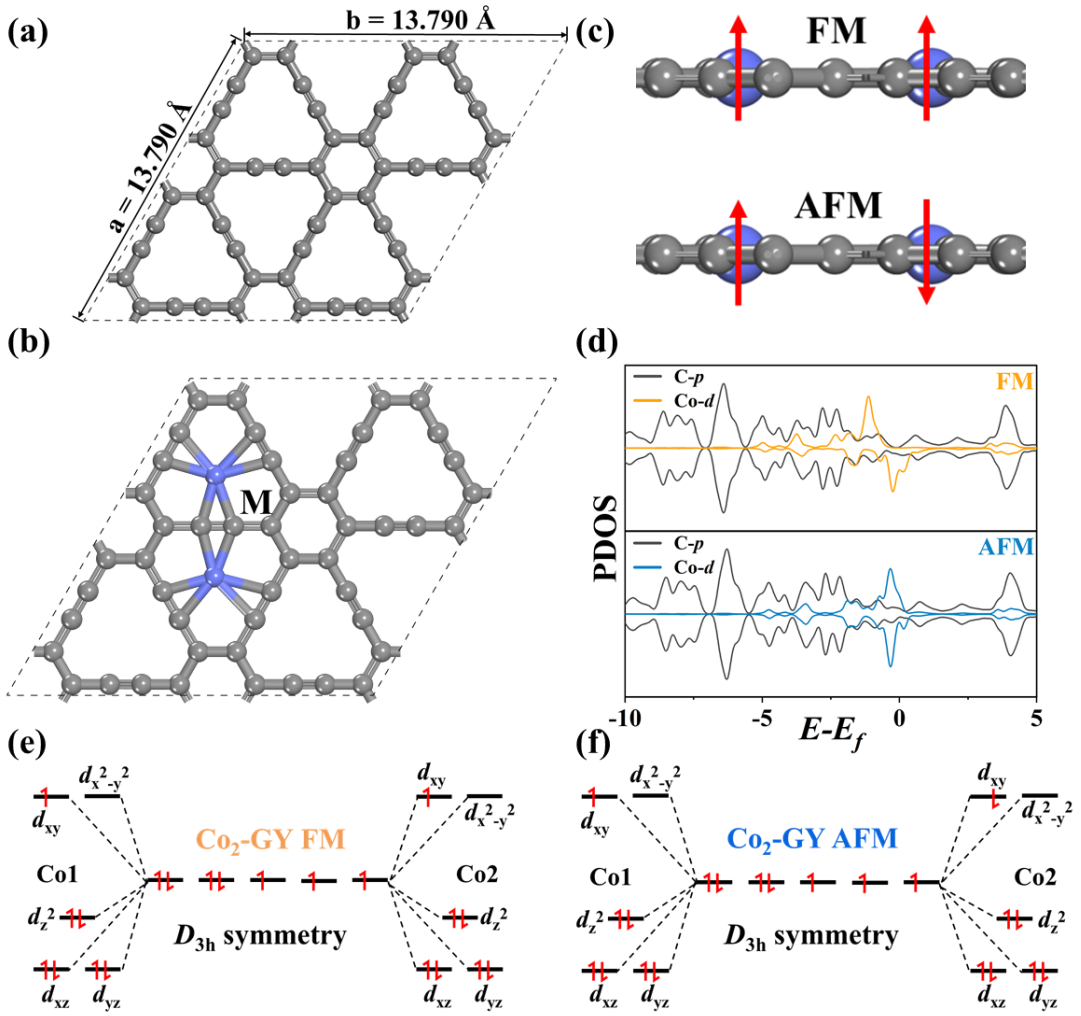

Figure 1. (a) The optimized structure of GY. (b) The structure scheme of M_2-GY. (c) The scheme of FM and AFM M_2-GYs. (d) The PDOS of *d* orbitals in Co on ground states FM and AFM Co_2-GY. e-f) The schematic diagrams of *d* orbitals splitting and spin electron arrangement in each Co for FM and AFM Co_2-GY.

The thermodynamic stability of ground states Fe_2/Co_2-GY with both FM and AFM configurations was thoroughly examined through the analysis of binding energies, as depicted in **Figure 2a**. The results reveal a notable absence of cluster formation for Fe/Co, as all binding energy values are consistently below zero (Fe: -4.34 for FM state, -4.32 for AFM state; Co: -5.37 for FM state, -5.31 for AFM state). These findings strongly suggest the feasibility of experimental realization of Fe_2/Co_2-GY. Comparatively, the interaction between cobalt (Co) and graphene (GY) exhibits a more pronounced binding affinity, owing to the considerably lower binding energies observed in both FM and AFM configurations. Notably, the stability characteristics of

Fe/Co are nearly indistinguishable between FM and AFM configurations. In addition, the stability of FM Fe/Co was basically same as that for AFM ones. These suggests the stability of magnetic metals is closely related to the classes of metals in DMACs.

3.2 CO Adsorption

According to Sabatier principle,[50] achieving a moderate bond strength between the reactant CO and M_2-GY emerges as a pivotal prerequisite for catalyzing CORR. Examining **Table S5**, we observe that when a single CO molecule is adsorbed, the magnetic ground state remains unaltered for Fe_2-GY, whereas for Co_2-GY, the magnetic exchange shifts from FM to PM states. During the initial CO adsorption event, Fe_2-GY features an adsorption energy of -1.59 eV, while Co_2-GY records -1.40 eV with a magnetic inversion. Similarly, upon the second CO adsorption, the adsorption energy for Fe_2-GY reaches -2.19 eV, accompanied by a magnetic phase shift from FM state to diamagnetic (DM) state, leading to pronounced CO poisoning. This underscores the unsuitability of Fe_2-GY to catalyzing CORR. In contrast, Co_2-GY exhibits a slightly reduced adsorption strength, decreasing from -1.40 eV to -1.25 eV, while maintaining an AFM state. This suggests that Co_2-GY holds promise for exhilarating research in eCORR . Moreover, it is essential to highlight that the transformation of the magnetic phase significantly influences adsorption pathways in catalytic reactions. To assess the potential for competing hydrogen evolution reactions (HER) during eCORR, the adsorption energy of hydrogen on Co_2-GY, calculated based on the most-steady state principle, stood at 0.05 eV. This value is lower than the adsorption energies of the two CO molecules (-1.40 and -1.25 eV), indicating a preference for CO reduction. In general, when experimentally exposed to CO environment, both Co_2-GY and Fe_2-GY adsorbs two CO molecules. Co_2-GY has suitable adsorption property to catalyzing eCORR.

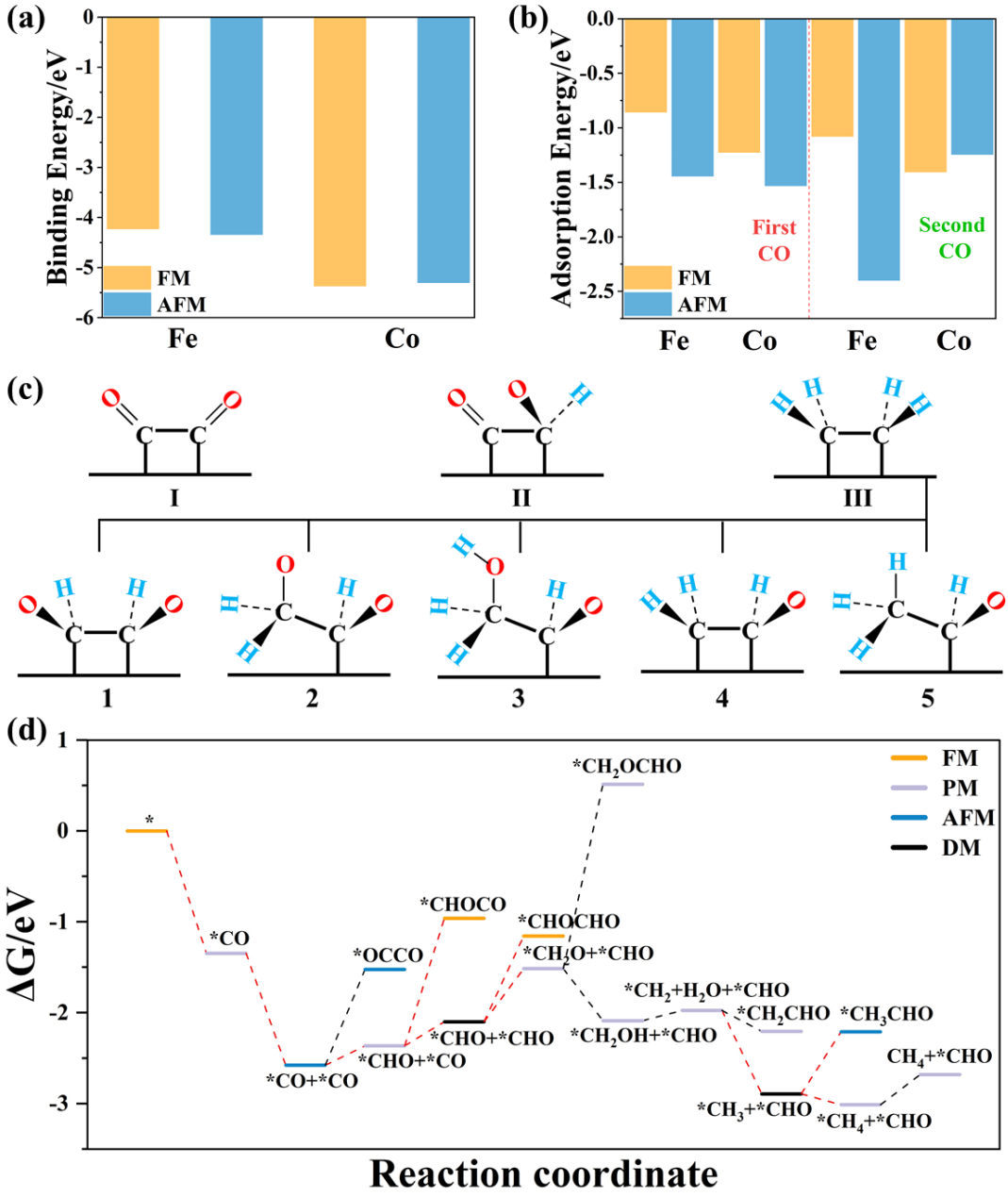

Figure 2. (a) The binding energy of Fe/Co, and (b) The adsorption energy of the first and second CO for Fe_2/Co_2-GY with FM and AFM. (c) The schematic diagram of three traditional C-C coupling mechanisms and five possible coupling modes. (d) The corresponding reaction pathways via the above C-C coupling mechanisms.

3.3 C-C Coupling Mechanisms and C_2 Reaction Pathway

The C-C coupling is a crucial step for the formation of high-value added multi-carbon (C_{2+}) chemicals via CO reduction. Nevertheless, electrocatalytic C-C coupling remains

a challenging experimental objective. The diversification of reactive sites and coupling mechanisms plays a crucial role in promoting C-C coupling reactions. Typically, Copper catalysts are prevalent in CORR/CO_2RR, with Cu-Cu sites spaced at approximately 2.7 Å.[51-54] Frustrated Lewis pairs (FLP) exhibit nonmetal-nonmetal active sites, typically with B-N distances ranging from 3.2 to 4.1 Å.[55] Whether it is possible for two Co site with the distance of 3.80 Å catalyze the coupling reaction of two adsorbed CO molecules under electrochemical condition? Therefore, we firstly conducted following coupling studies. C-C coupling requires a significant amount of energetic penalty, making it a potential limiting factor. Simplifying C-C coupling is essential to enhance C_2 product yields. Three mechanisms (I-III) of C-C coupling (see **Figure 2c**), involving CO* dimerization, CO* + CHO* coupling, and carbine (CH_2*) dimerization, have been extensively studied both theoretically and experimentally to date. To realize the three mechanisms, the reaction pathways (A-C) based on the most stable structures in both FM and AFM states were described in **Figure 2d** and structure energies of all intermediates were counted in **Table S6**. (I) CO* Dimerization: A free energy of 1.00 eV is needed to accomplish this step on Co_2-GY without inducing magnetic conversion. In Pathway A, dual CO* coupling was the potential-limiting step (PLS) and the magnetic transition sequence along this pathway was: FM - PM - AFM - AFM. (II) CO* + CHO* Coupling: In Pathway B, achieving this step involved a 1.40 eV increase in free energy and a transition from PM to FM, making it a potential limiting step. The magnetism transition sequence throughout this process was FM - PM - AFM - PM - FM. (III) CH_2* Dimerization: Unfortunately, Co_2-GY with adsorbed CH_2 was not in the most stable state; instead, Co_2-GY adsorbing CH_3 in the sixth hydrogenation (**Figure 2d** and **Table S6**) emerged as the more stable option, suggesting that CH_2* dimerization is not practically feasible. The challenging reality is that CO* dimerization was the most favorable, but its realization incurred a substantial cost due to the 1.00 eV free energy constraint. Under this situation, five possible coupling pathways as follows: **(1)** CHO* dimerization, **(2)** CH_2O* + CHO* coupling, **(3)** CH_2*OH + CHO* coupling, **(4)** CH_2* + CHO* coupling and **(5)** CH_3* + CHO* coupling, were further identified in Pathway C (see **Figure 2c-2d)**. Within this context,

C-C coupling remained unachievable due to a substantial increase in free energy by 0.94 and 2.03 eV in modes 1 and 2, respectively. These coupling steps were all PLSs, accompanied by magnetic transitions from DM to FM and PM to PM. Additionally, the coupling between CH_2OH* and CHO* in mode 3 could not be realized due to the significant steric hindrance posed by CH_2OH*. Furthermore, in mode 5, the free energy required for C-C coupling was only 0.68 eV (PLS, DM - AFM), significantly lower than the 0.94 eV threshold, indicating that C-C coupling became considerably less challenging. Intriguingly, in mode 4, the reaction's free energy for CH_2* + CHO* coupling (PM - PM) was -0.23 eV, suggesting that this coupling step was thermodynamically spontaneous. This spontaneity was due to a combination of reduced steric hindrance (see **Figure S6**) and enhanced attraction between the double carbon atoms during pre-coupling, as indicated by Bader charge analysis (see **Table S7**). In this pathway, the PLS is no longer the C-C coupling step but the hydrogenation from CHO* + CHO* to CH_2O* + CHO*, involving a magnetic transition from DM to PM and an associated reaction energy of 0.58 eV (< 0.68 eV in mode 5). As a result, a highly efficient and new C-C coupling reaction pathway (CH_2* + CHO* coupling) has emerged, featuring magnetic transitions in the sequence FM - PM - AFM - PM - DM - PM - PM - PM - PM. Similarly, when considering only FM or AFM, the optimal C-C coupling mechanisms were either CH_2O* + CO* coupling or CHOH* + CHO* coupling, with the potential limiting step being the formation of CHO* + CO* (0.47 eV) or CHOH* + CHO* (0.77 eV), as shown in **Figure S7-S8**. All structure energies of intermediates are detailed in **Table S8**. Hence, the magnetic transition is also a significant factor to affect C-C coupling mechanism and pathway.

Furthermore, the PM H_2CCHO* was selected as the precursor of C_2 products on FM and AFM Co_2-GY (see **Figure S9)**, and all the most stable intermediates were shown in **Table S9**. The initial protonation of PM H_2CCHO* occurs on the C or O atoms, resulting in H_2CCHOH*, H_2CCH_2O* or H_3CCHO* intermediates. Among them, the first protonation of PM H_2CCHO* to FM H_3CCHO* was thermodynamically favorable with the free energy of -0.45 eV. Then, a proton attacked the C or O atoms of FM H_3CCHO* to form two kinds of intermediates, i.e., H_3CCH_2O* and H_3CCHOH*. In

this regard, the AFM H_3CCH_2O* possessed optimal stability with the uphill trend of ΔG = 0.12 eV, which is endothermal with non-magnetic phase transition. Similarly, further hydrogenation of AFM H_3CCH_2O* results in the most stable FM H_3CCH_2OH* with the downhill trend of ΔG = -0.28 eV among two classes of intermediates: H_3CCH_2OH* and H_3CCH_3 + O*. In the end, the desorption of adsorbed CH_3CH_2OH required 0.32 eV free energy, suggesting the desorption is relatively easy. Therefore, combining the results of **Figure 2d** and **Figure S9**, the CH_3CH_2OH is the final C_2 product via CH_2* + CHO* coupling in the most steady state pathway, portrayed in **Figure 3a**, i.e., * → CO* → CO* + CO* → CHO* + CO* → CHO* + CHO* → CH_2O* + CHO* → CH_2OH* + CHO* → CH_2* + CHO* + H_2O → H_2CCHO* → H_3CCHO* → H_3CCH_2O* → H_3CCH_2OH* → H_3CCH_2OH + * with transition process of magnetic phase: FM - PM - AFM - PM - DM - PM - PM - PM - PM - FM - AFM - FM - FM (Magnetic moment of each intermediate is listed in **Table S10**), in which the formation of PM CH_2O* + CHO* was as the PLS with boost of 0.58 eV free energy. All the most stable structures of intermediates in this pathway were enumerated in **Figure 3c**. The reaction pathways of only considering FM or AFM based on the most stable intermediates were exhibited in **Figure S10-S11** and structural energies were shown in **Table S11**, revealing the HOH_2CCH_2OH or CH_3CH_3 was the final C_2 product with the formation of CHO* + CO* (0.47 eV) or CHOH* + CHO* (1.00 eV) as the PLS. These indicate a surprising conclusion was obtained, i.e., the magnetic phase transition does change the C_2 reaction pathway and activity.

3.4 Electrochemical Condition-Dependent Spin Dynamic and Catalytic Performance for C_2 pathway

Experimentally, the activity and selectivity to C_2 products via CORR are significantly influenced by pH values of solvent and applied potential due to the variation of intermediates. Herein, the same reaction pathway as above study was selected. **Figure S13-S14** shown the potential dependence of energies and adsorption energy on bare Co_2-GY and intermediates (see **Figure S13** are **Table S12**). Under applied potential, both Co_2-GY and intermediates undergoes magnetic transition, and thereby induces different adsorption conformations of oxygenated species, inevitably affecting the reactivity of

C_2-pathway. At constant potential model, according to the equation: U/RHE = U/SHE + $k_B T$ln(10)pH/e, when U/RHE is fixed, the U/SHE is the function of pH. Thus, reaction property to C_2 products is also highly dependent on pH values.

Three environments (pH = 0, 7, and 14) were selected to investigate C_2-catalytic activity and magnetism transitions under acidic, neutral, and basic conditions, as shown in **Figure 3a**. The structure energies were counted in **Table S13**. At pH = 0, the CH_2* + CHO* coupling occurred with a 0.31 eV free energy change, distinct from the vacuum conditions. Nevertheless, other steps' free energy changes and the magnetic ground states of all intermediates remained like those in vacuum. The PLS still belonged to the formation of CH_2O* + CHO* with free energy change of 0.54 eV (< 0.58 eV in vacuum). At pH = 7, the free energy changes for two steps, the creation of H_2CCHO* and the removal of adsorbed H_3CCH_2OH, are significantly different from those in a vacuum (0.24 and -0.05 eV versus -0.23 and 0.32 eV). Hence, the transition process of magnetic phase was as follows: FM - PM - AFM - FM - DM - PM - FM - PM - PM - FM - DM - PM - FM. While the PLS was also the production of CH_2O* + CHO* with 0.50 eV (< 0.58 eV in vacuum) reaction energy. Likewise, at pH = 14, compared to reaction energies in a vacuum, both the generation of H_3CCH_2O* and the removal of adsorbed H_3CCH_2OH shift from non-spontaneous to spontaneous (-0.09 eV from 0.12 eV; -0.35 eV from 0.32 eV), whereas the formation of H_2CCHO* changes from -0.23 eV to 0.29 eV. In whole pathway, the step, CHO* + CHO* → CH_2O* + CHO*, was still as the PLS with a rise of 0.50 eV free energy, which lower than 0.58 eV in vacuum. Moreover, the transition process of magnetic phase was FM - PM - AFM - PM - DM - PM - FM - PM - PM - FM - DM - FM - FM, in which three of them differed from those in vacuum. Hence, adjusting pH serves as a crucial means to control C_2-catalytic properties and induce magnetic transitions in the reaction. Moreover, C_2 reaction activity was similar in neutral and alkaline solvents, slightly outperforming acidic solvents. Considering the crucial role of external potential in electrocatalysis, it induces structural changes in reaction intermediates. As shown in **Figure S12**, at different potentials (-0.973 V/SHE and 1.575 V/SHE), the orientations of C-O bonds in the intermediates CH_2O* and CHO* change. This variation may have implications for subsequent coupling reactions.

Subsequently, we evaluated the initial potential for the C_2 reaction on the catalyst at different pH values, as illustrated in **Figure 3b**. The influence of pH on the applied potential for the C_2 reaction was found to be extremely subtle, with a difference of approximately 0.001 V observed across diverse pH levels. **Figure 3b** vividly demonstrates that the applied potential exerts a substantial promotion on the catalytic reaction activity. Notably, since desorption belongs to the realm of chemical processes, the applied potential lacks the ability to modify its thermodynamic tendency. Consequently, at U = -0.50 V/RHE and pH = 0, the desorption of ethanol remains an endothermic process. It is worth noting that the presence of adsorbates typically triggers alterations in the point of zero charge (PZC) and the capacitance of the electrochemical surface. In comparison to the exposed Co_2-GY, each reduced intermediate exhibits a negative shift in their respective PZCs, signifying an enhanced surface electron release capability and, thus, improved reduction performance (**Table S14**). During the PZC transition, CO adsorption slightly raises capacitance, but as reduction continues, capacitance slightly decreases. The adsorption behavior of reactants is notably affected by both the PZC transition and capacitance changes, as illustrated in Figure S14. In contrast to the bare Co_2-GY surface, the PZC transition for the key adsorbates CH_2O* + CHO* is relatively small, approximately 0.03 V. Consequently, within the same potential range (-3 V to 2 V), their adsorption fluctuations exhibit considerably more pronounced variations.

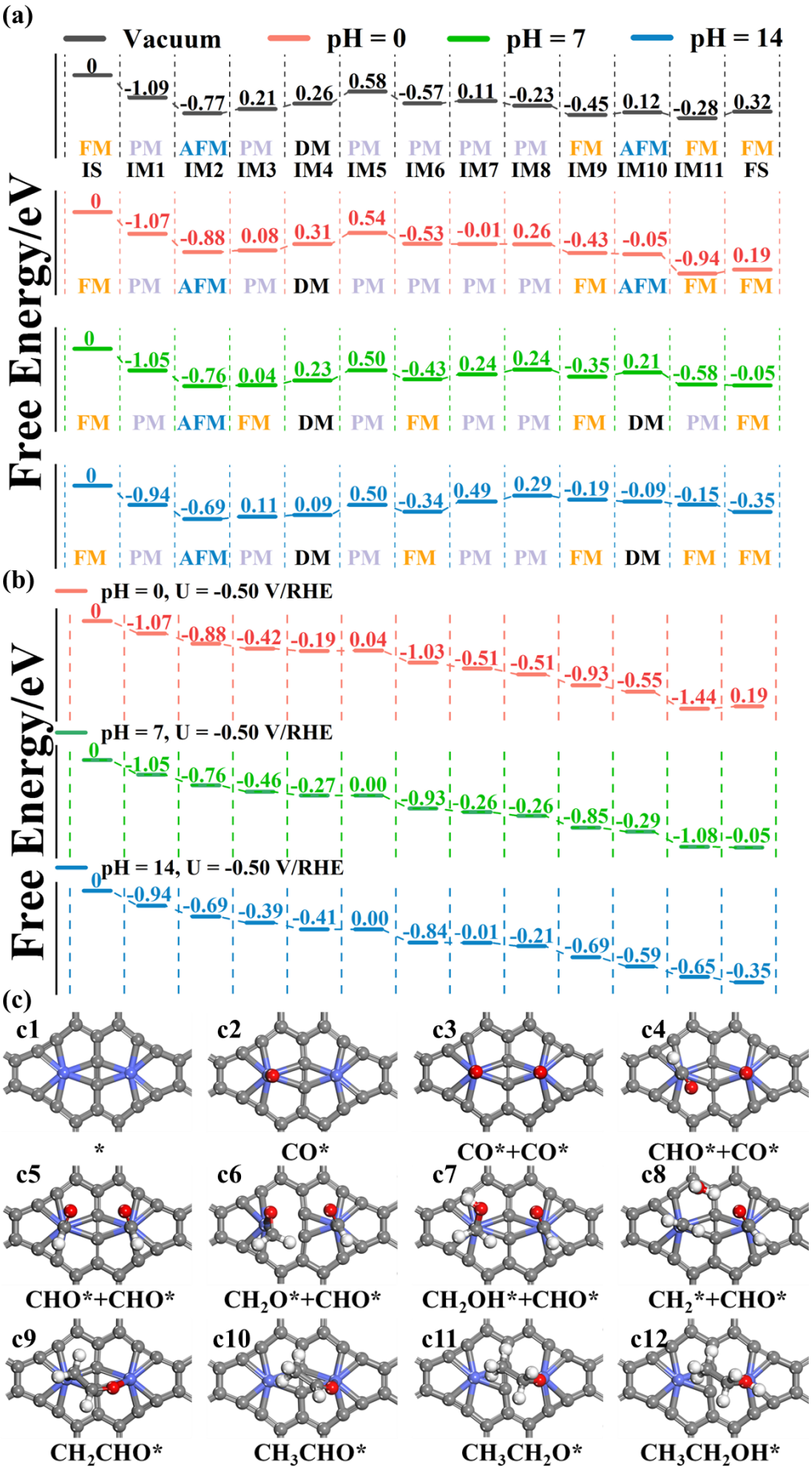

Figure 3. (a) The whole most-steady state C_2 reaction pathway and magnetic phase transition via CH_2* + CHO* coupling mechanism in vacuum and implicit solvent with pH = 0, 7 and 14 (IS, IM and FS represent initial state, intermediate and final state, respectively). (b) Free energy profile of C_2 reaction pathway on Co_2-GY at U = -0.50 V/RHE, pH = 0; U = -0.50 V/RHE, pH = 7 and U = -0.50 V/RHE, pH = 14. (c) All the most stable structures of intermediates in the most-steady state C_2 reaction pathway in vacuum(c1 corresponds to IS and FS in Figure a, while c2-12 correspond to IM1-11 in Figure a, respectively).

3.5 Electrochemical Condition-Dependent Spin Dynamic and Catalytic Performance for C_1 pathway

Moreover, we evaluated the potential dependence of reaction pathway of C_1 products based on the steadiest state structures. In vacuum, CH_3OH was the final C_1 product in the most stable pathway, i.e., * → CO* → CHO* → CHOH* → CH_2OH* → CH_3OH* → CH_3OH + *, accompanying with the magnetic transition pathway: FM - PM - FM - DM - FM - FM - FM (see **Table S15**). Herein, the hydrogenation of CO* to form CHO* was the PLS with the uphill trend of ΔG = 0.48 eV (see **Figure 4a** and **Table S16)**. The most stable intermediate structures in this pathway are shown in **Figure 4c**. **Figure S15-S16** illustrated the total energies of five types of intermediates and their adsorption energies under different magnetic states at various applied potentials (see **Figure S15** and **Table S17**). These results reveal the significant impact of the applied potential on both the magnetic ground state and the adsorption interactions between Co_2-GY and adsorbed species. Additionally, employing a constant potential model, we chose three solvent environments at pH levels of 0, 7, and 14 to assess the influence of pH on catalytic activity and magnetic transitions (see **Figure 4a** and **Table S18**). In the acidic environment, the change of reaction free energy is different from that in vacuum, including the change of PLS (from the formation of CHO* to the formation of CH_3OH*), and the desorption of adsorbed CH_3OH, which became spontaneous with a -0.18 eV free energy, in contrast to the 0.33 eV in vacuum. In this pathway, the formation of CH_3OH* exhibited lower PLS with a

0.27 eV free energy (compared to 0.49 eV in vacuum, the formation of CHO*). Unfortunately, the magnetism conversion process remained consistent with that in a vacuum. At pH = 7 and 14, the free energy trends for all reaction steps resembled those in a vacuum. The PLSs were not the formation of CHO* or CH_3OH*, but rather the generation of CHOH* with free energies of 0.51 eV and 0.73 eV, both higher than the 0.49 eV value observed in a vacuum. Notably, there were distinct sequences of magnetic transitions at pH = 7 (FM - PM - DM - PM - DM - FM - FM) compared to those observed under vacuum conditions, while the magnetic transition sequence remains unchanged at pH = 14 (FM - PM - FM - DM - FM - FM - FM). In general, both the solvent and pH levels synergistically influence C_1 reaction activity and spin flipping. Specifically, C_1 activity is highest in acidic conditions and lowest in alkaline environments. In contrast to the C_2 reaction, the influence of pH on the applied potential for the C_1 reaction is significant, as depicted in **Figure 4b**. At pH = 0, the applied potential (U = -0.23 V/RHE) is lower than the -0.50 V/RHE observed for the C_2 reaction, indicating that, under this pH condition, the C_1 reaction exhibits superior performance compared to the C_2 reaction. As the pH increases, the applied potential undergoes a sharp increase, reaching -1.27 V/RHE at pH = 7 and -1.73 V/RHE at pH = 14. This remarkable shift can be attributed to the changes induced by pH-dependent potential-limiting steps. Furthermore, the PZC and capacitance of the electrochemical surface experience modifications in the context of the C_1 reaction. Additionally, each intermediate displays a negative shift in their respective PZCs, as indicated in **Table S19**. Among the intermediate species, CHOH* undergoes the most significant PZC transition, approximately 0.37 V, in comparison to the bare Co_2-GY surface. Consequently, the adsorption energy of CHO* exhibits a more prominent increase as the external potential rises, resulting in a difference of approximately 3 eV in its adsorption energy within the same potential range (-3 V to 2 V).

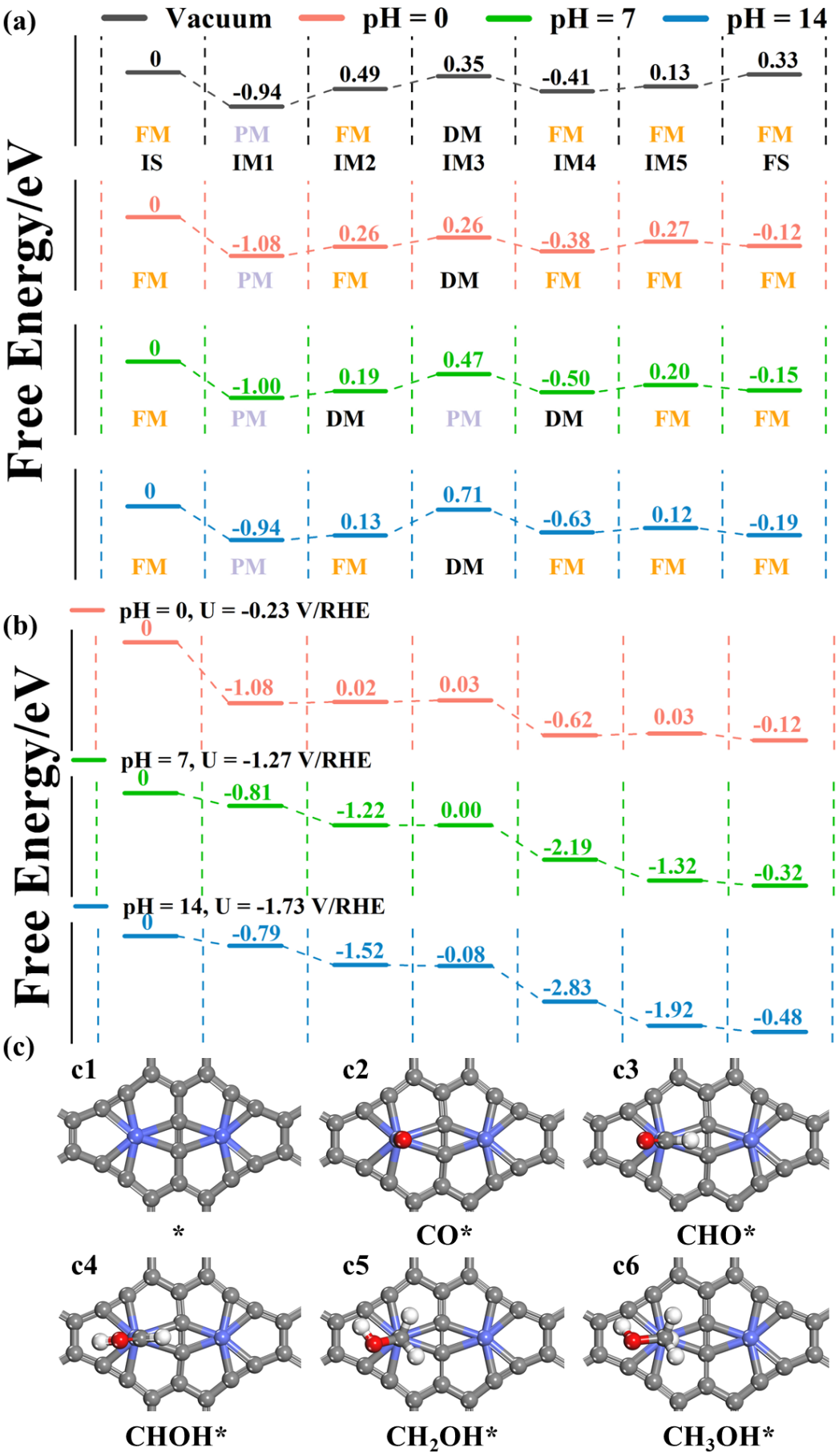

448

Figure 4. (a) The most-steady state C_1 reaction pathway and magnetic phase transition in vacuum and implicit solvent with pH = 0, 7 and 14 (IS, IM and FS represent initial state, intermediate and final state, respectively). (b) Free energy profile of C_1 reaction pathway on Co_2-GY at U = -0.23 V/RHE, pH = 0; U = -1.27 V/RHE, pH = 7 and U = -1.73 V/RHE, pH = 14. c) All the most stable structures of intermediates in the most-steady state C_1 reaction pathway in vacuum (c1 corresponds to IS and FS in Figure a, while c2-6 correspond to IM1-5 in Figure a, respectively).

4. Conclusions

In summary, we screened out the Co_2-GY to systematically investigate the synergetic effect of the applied potential and acidy on spin dynamic and catalytic performance (especially for selectivity) for C_2/C_1 products of CO electroreduction via the constant-potential implicit solvent model. Our findings indicate that under acidic condition, Co_2-GY exhibits high CH_3OH selectivity (around 99%) and an activity of 0.27 eV, while under basic conditions, it achieves a CH_3CH_2OH selectivity of over 99% and an activity of 0.50 eV. During electrocatalysis, Co_2-GY displays intriguing spin dynamics with magnetic exchange between two Co ions, following the pathway: FM - PM - AFM - PM - DM - PM - PM - PM - PM - FM - AFM - FM - FM. This leads to a novel and efficient C-C coupling mechanism involving the interaction between CH_2* and CHO*. Under the applied potential, C_2 activity improves (0.58 → 0.50 eV) under neutral and alkaline conditions, and (0.58 → 0.54 eV) in an acidic solvent. The spin dynamic proceed as follows: FM - PM - AFM - PM - DM - PM - PM - PM - PM - FM - AFM - FM - FM at pH = 0, FM - PM - AFM - FM - DM - PM - FM - PM - PM - FM - DM - PM - FM. at pH = 7 and FM - PM - AFM - PM - DM - PM - FM - PM - PM - FM - DM - FM - FM at pH = 14. For the C_1 Pathway, the optimal CH_3OH product formation (0.48 eV for CHO* formation) occurs through spin dynamic of FM - PM - FM - DM - FM - FM - FM. Under the applied potential, C_1 activity decreases (0.49 → 0.51/0.73 eV) under neutral and alkaline conditions, while it improves (0.49 → 0.27 eV) under acidic conditions. The corresponding spin dynamics are presented as follows: FM - PM - FM - DM - FM - FM - FM in pH = 0, FM - PM - DM - PM - DM - FM - FM at pH =

7 and FM - PM - FM - DM - FM - FM - FM at pH = 14. These findings aid in understanding spin dynamics during electrocatalytic reduction on paramagnetically heterogeneous catalysts.

Supporting Information

Supporting Information is available from the Wiley Online Library or from the author.

Acknowledgements

This work was supported by the National Natural Science Foundation of China (Grant No: 22022108, 22072135, 21671172), Zhejiang Provincial Natural Science Foundation of China (Grant No: LR19B010001), Natural Science Foundation of Shandong Province (ZR2020ZD35).

Conflict of interest

The authors declare no conflict of interest

Data Availability Statement

The data that support the findings of this study are available from the corresponding author upon reasonable request.

Reference

1. Wu, Y.; Chen, C.; Yan, X.; Wu, R.; Liu, S.; Ma, J.; Zhang, J.; Liu, Z.; Xing, X.; Wu, Z.; Han, B., Enhancing CO(2) electroreduction to CH(4) over Cu nanoparticles supported on N-doped carbon. *Chem Sci* **2022,** *13* (28), 8388-8394.

2. Hung, S. F.; Xu, A.; Wang, X.; Li, F.; Hsu, S. H.; Li, Y.; Wicks, J.; Cervantes, E. G.; Rasouli, A. S.; Li, Y. C.; Luo, M.; Nam, D. H.; Wang, N.; Peng, T.; Yan, Y.; Lee, G.; Sargent, E. H., A metal-supported single-atom catalytic site enables carbon dioxide hydrogenation. *Nat Commun* **2022,** *13* (1), 819.

3. Li, X.; Sun, Y.; Xu, J.; Shao, Y.; Wu, J.; Xu, X.; Pan, Y.; Ju, H.; Zhu, J.; Xie, Y., Selective visible-light-driven photocatalytic CO2 reduction to CH4 mediated by atomically thin CuIn5S8 layers. *Nature Energy* **2019,** *4* (8), 690-699.

4. Wang, T.; Sun, F. L.; Liu, S. J.; Zhuang, G. L.; Li, B. X., Dioxygen-enhanced CO₂ photoreduction on TiO₂ supported Cu single-atom sites. *APPLIED CATALYSIS B-ENVIRONMENTAL* **2023,** *325*.

5. Kong, S.; Lv, X.; Wang, X.; Liu, Z.; Li, Z.; Jia, B.; Sun, D.; Yang, C.; Liu, L.; Guan, A.; Wang, J.; Zheng, G.; Huang, F., Delocalization state-induced selective bond breaking for efficient methanol electrosynthesis from CO2. *Nature Catalysis* **2022,** *6* (1), 6-15.

6. Li, P.; Bi, J.; Liu, J.; Zhu, Q.; Chen, C.; Sun, X.; Zhang, J.; Han, B., In situ dual doping for constructing efficient CO(2)-to-methanol electrocatalysts. *Nat Commun* **2022,** *13* (1), 1965.

7. Vasileff, A.; Zhu, Y.; Zhi, X.; Zhao, Y.; Ge, L.; Chen, H. M.; Zheng, Y.; Qiao, S. Z., Electrochemical Reduction of CO(2) to Ethane through Stabilization of an Ethoxy Intermediate. *Angew Chem Int Ed Engl* **2020,** *59* (44), 19649-19653.

8. Chen, P.; Zhang, P.; Kang, X.; Zheng, L.; Mo, G.; Wu, R.; Tai, J.; Han, B., Efficient Electrocatalytic Reduction of CO(2) to Ethane over Nitrogen-Doped Fe(2)O(3). *J Am Chem Soc* **2022,** *144* (32), 14769-14777.

9. Ou, H.; Li, G.; Ren, W.; Pan, B.; Luo, G.; Hu, Z.; Wang, D.; Li, Y., Atomically Dispersed Au-Assisted C-C Coupling on Red Phosphorus for CO(2) Photoreduction to C(2)H(6). *J Am Chem Soc* **2022,** *144* (48), 22075-22082.

10. Ding, L.; Zhu, N.; Hu, Y.; Chen, Z.; Song, P.; Sheng, T.; Wu, Z.; Xiong, Y., Over 70 % Faradaic Efficiency for CO(2) Electroreduction to Ethanol Enabled by Potassium Dopant-Tuned Interaction between Copper Sites and Intermediates. *Angew Chem Int Ed Engl* **2022,** *61* (36), e202209268.

11. Li, Y. C.; Wang, Z.; Yuan, T.; Nam, D. H.; Luo, M.; Wicks, J.; Chen, B.; Li, J.; Li, F.; de Arquer, F. P. G.; Wang, Y.; Dinh, C. T.; Voznyy, O.; Sinton, D.; Sargent, E. H., Binding Site Diversity Promotes CO(2) Electroreduction to Ethanol. *J Am Chem Soc* **2019,** *141* (21), 8584-8591.

12. Guo, C.; Guo, Y.; Shi, Y.; Lan, X.; Wang, Y.; Yu, Y.; Zhang, B., Electrocatalytic Reduction of CO(2) to Ethanol at Close to Theoretical Potential via Engineering Abundant Electron-Donating Cu(delta+) Species. *Angew Chem Int Ed Engl* **2022,** *61* (32), e202205909.

13. Zhuo, T.-C.; Song, Y.; Zhuang, G.-L.; Chang, L.-P.; Yao, S.; Zhang, W.; Wang, Y.; Wang, P.; Lin, W.; Lu, T.-B.; Zhang, Z.-M., H-Bond-Mediated Selectivity Control of Formate versus CO during CO2 Photoreduction with Two Cooperative Cu/X Sites. *Journal of the American Chemical Society* **2021,** *143* (16), 6114-6122.

14. Sun, F.-l.; Fang, Q.-j.; Yu, Y.-f.; Zhang, W.; Pan, J.-k.; Chen, W.-X.; Zhuang, G.-l., Enhancing mechanism of electron-deficient p states on photocatalytic activity of g-C3N4 for CO2 reduction. *Journal*

of Materials Chemistry A **2022,** *10* (17), 9565-9574.
15. Zhang, X. Y.; Li, W. J.; Chen, J.; Wu, X. F.; Liu, Y. W.; Mao, F.; Yuan, H. Y.; Zhu, M.; Dai, S.; Wang, H. F.; Hu, P.; Sun, C.; Liu, P. F.; Yang, H. G., In Operando Identification of In Situ Formed Metalloid Zinc(delta+) Active Sites for Highly Efficient Electrocatalyzed Carbon Dioxide Reduction. *Angew Chem Int Ed Engl* **2022,** *61* (28), e202202298.
16. Li, J.; Zeng, H.; Dong, X.; Ding, Y.; Hu, S.; Zhang, R.; Dai, Y.; Cui, P.; Xiao, Z.; Zhao, D.; Zhou, L.; Zheng, T.; Xiao, J.; Zeng, J.; Xia, C., Selective CO(2) electrolysis to CO using isolated antimony alloyed copper. *Nat Commun* **2023,** *14* (1), 340.
17. Player, T. C.; Hore, P. J., Source of magnetic field effects on the electrocatalytic reduction of CO(2). *J Chem Phys* **2020,** *153* (8), 084303.
18. Pan, H.; Xiao, X.; Hu, B.; Shen, Y.; Wang, M., Generating Huge Magnetocurrent by Using Spin-Dependent Dehydrogenation Based on Electrochemical System. *The Journal of Physical Chemistry C* **2017,** *121* (51), 28420-28424.
19. Kumar, A.; Capua, E.; Vankayala, K.; Fontanesi, C.; Naaman, R., Magnetless Device for Conducting Three-Dimensional Spin-Specific Electrochemistry. *Angew Chem Int Ed Engl* **2017,** *56* (46), 14587-14590.
20. Beardmore, J. P.; Antill, L. M.; Woodward, J. R., Optical Absorption and Magnetic Field Effect Based Imaging of Transient Radicals. *Angew Chem Int Ed Engl* **2015,** *54* (29), 8494-7.
21. Zeng, Z.; Zhang, T.; Liu, Y.; Zhang, W.; Yin, Z.; Ji, Z.; Wei, J., Magnetic Field-Enhanced 4-Electron Pathway for Well-Aligned Co(3) O(4) /Electrospun Carbon Nanofibers in the Oxygen Reduction Reaction. *ChemSusChem* **2018,** *11* (3), 580-588.
22. Haberkorn, R., Density matrix description of spin-selective radical pair reactions. *Molecular Physics* **2006,** *32* (5), 1491-1493.
23. Johnson, R. C.; Merrifield, R. E., Effects of Magnetic Fields on the Mutual Annihilation of Triplet Excitons in Anthracene Crystals. *Physical Review B* **1970,** *1* (2), 896-902.
24. Deviers, J.; Cailliez, F.; de la Lande, A.; Kattnig, D. R., Anisotropic magnetic field effects in the re-oxidation of cryptochrome in the presence of scavenger radicals. *J Chem Phys* **2022,** *156* (2), 025101.
25. McLauchlan, K. A.; Steiner, U. E., Invited article. *Molecular Physics* **1991,** *73* (2), 241-263.
26. Xu, J.; Jarocha, L. E.; Zollitsch, T.; Konowalczyk, M.; Henbest, K. B.; Richert, S.; Golesworthy, M. J.; Schmidt, J.; Dejean, V.; Sowood, D. J. C.; Bassetto, M.; Luo, J.; Walton, J. R.; Fleming, J.; Wei, Y.; Pitcher, T. L.; Moise, G.; Herrmann, M.; Yin, H.; Wu, H.; Bartolke, R.; Kasehagen, S. J.; Horst, S.; Dautaj, G.; Murton, P. D. F.; Gehrckens, A. S.; Chelliah, Y.; Takahashi, J. S.; Koch, K. W.; Weber, S.; Solov'yov, I. A.; Xie, C.; Mackenzie, S. R.; Timmel, C. R.; Mouritsen, H.; Hore, P. J., Magnetic sensitivity of cryptochrome 4 from a migratory songbird. *Nature* **2021,** *594* (7864), 535-540.
27. Pan, H.; Jiang, X.; Wang, X.; Wang, Q.; Wang, M.; Shen, Y., Effective Magnetic Field Regulation of the Radical Pair Spin States in Electrocatalytic CO(2) Reduction. *J Phys Chem Lett* **2020,** *11* (1), 48-53.
28. Sun, Z.; Lin, L.; He, J.; Ding, D.; Wang, T.; Li, J.; Li, M.; Liu, Y.; Li, Y.; Yuan, M.; Huang, B.; Li, H.; Sun, G., Regulating the Spin State of Fe(III) Enhances the Magnetic Effect of the Molecular Catalysis Mechanism. *J Am Chem Soc* **2022,** *144* (18), 8204-8213.
29. Yu, L.; Li, F.; Zhao, J.; Chen, Z., Revisiting catalytic performance of supported metal dimers for oxygen reduction reaction via magnetic coupling from first principles. *Advanced Powder Materials* **2022,** *1* (3).

30. Dang, Q.; Tang, S.; Liu, T.; Li, X.; Wang, X.; Zhong, W.; Luo, Y.; Jiang, J., Regulating Electronic Spin Moments of Single-Atom Catalyst Sites via Single-Atom Promoter Tuning on S-Vacancy MoS(2) for Efficient Nitrogen Fixation. *J Phys Chem Lett* **2021,** *12* (34), 8355-8362.
31. Kresse, G.; Furthmüller, J., Efficient iterative schemes for ab initio total-energy calculations using a plane-wave basis set. *Physical Review B* **1996,** *54* (16), 11169-11186.
32. Perdew, J. P.; Burke, K.; Ernzerhof, M., Generalized gradient approximation made simple (vol 77, pg 3865, 1996). *PHYSICAL REVIEW LETTERS* **1997,** *78* (7), 1396-1396.
33. Ernzerhof, M.; Perdew, J. P., Generalized gradient approximation to the angle- and system-averaged exchange hole. *The Journal of Chemical Physics* **1998,** *109* (9), 3313-3320.
34. Blochl, P. E., Projector augmented-wave method. *Phys Rev B Condens Matter* **1994,** *50* (24), 17953-17979.
35. Kresse, G.; Joubert, D., From ultrasoft pseudopotentials to the projector augmented-wave method. *PHYSICAL REVIEW B* **1999,** *59* (3), 1758-1775.
36. Monkhorst, H. J.; Pack, J. D., Special points for Brillouin-zone integrations. *Physical Review B* **1976,** *13* (12), 5188-5192.
37. Grimme, S.; Antony, J.; Ehrlich, S.; Krieg, H., A consistent and accurate ab initio parametrization of density functional dispersion correction (DFT-D) for the 94 elements H-Pu. *The Journal of Chemical Physics* **2010,** *132* (15), 154104.
38. Grimme, S.; Ehrlich, S.; Goerigk, L., Effect of the damping function in dispersion corrected density functional theory. *J Comput Chem* **2011,** *32* (7), 1456-65.
39. Yang, J.; Liu, W.; Xu, M.; Liu, X.; Qi, H.; Zhang, L.; Yang, X.; Niu, S.; Zhou, D.; Liu, Y.; Su, Y.; Li, J. F.; Tian, Z. Q.; Zhou, W.; Wang, A.; Zhang, T., Dynamic Behavior of Single-Atom Catalysts in Electrocatalysis: Identification of Cu-N(3) as an Active Site for the Oxygen Reduction Reaction. *J Am Chem Soc* **2021,** *143* (36), 14530-14539.
40. Dudarev, S. L.; Botton, G. A.; Savrasov, S. Y.; Humphreys, C. J.; Sutton, A. P., Electron-energy-loss spectra and the structural stability of nickel oxide: An LSDA+U study. *Physical Review B* **1998,** *57* (3), 1505-1509.
41. Zhang, W.; Sun, F.-l.; Zhang, X.-l.; Zhao, S.-t.; Chen, W.-x.; Zhuang, G.-l., Mechanical-Effect descriptor for oxygen reduction reaction and hydrogen evolution reaction on Single-Atomic Ni-Graphene catalysts. *Fuel* **2024,** *355*.
42. Cococcioni, M.; de Gironcoli, S., Linear response approach to the calculation of the effective interaction parameters in theLDA+Umethod. *Physical Review B* **2005,** *71* (3).
43. Handy, N. C.; Cohen, A. J., Left-right correlation energy. *Molecular Physics* **2009,** *99* (5), 403-412.
44. Ye, S.; Neese, F., Accurate modeling of spin-state energetics in spin-crossover systems with modern density functional theory. *Inorg Chem* **2010,** *49* (3), 772-4.
45. Nørskov, J. K.; Rossmeisl, J.; Logadottir, A.; Lindqvist, L.; Kitchin, J. R.; Bligaard, T.; Jónsson, H., Origin of the Overpotential for Oxygen Reduction at a Fuel-Cell Cathode. *The Journal of Physical Chemistry B* **2004,** *108* (46), 17886-17892.
46. Duan, Z.; Henkelman, G., Theoretical Resolution of the Exceptional Oxygen Reduction Activity of Au(100) in Alkaline Media. *ACS Catalysis* **2019,** *9* (6), 5567-5573.
47. Hu, X.; Chen, S.; Chen, L.; Tian, Y.; Yao, S.; Lu, Z.; Zhang, X.; Zhou, Z., What is the Real Origin of the Activity of Fe-N-C Electrocatalysts in the O(2) Reduction Reaction? Critical Roles of Coordinating Pyrrolic N and Axially Adsorbing Species. *J Am Chem Soc* **2022,** *144* (39), 18144-18152.
48. Mathew, K.; Sundararaman, R.; Letchworth-Weaver, K.; Arias, T. A.; Hennig, R. G., Implicit

solvation model for density-functional study of nanocrystal surfaces and reaction pathways. *J Chem Phys* **2014,** *140* (8), 084106.
49. Mathew, K.; Kolluru, V. S. C.; Mula, S.; Steinmann, S. N.; Hennig, R. G., Implicit self-consistent electrolyte model in plane-wave density-functional theory. *J Chem Phys* **2019,** *151* (23), 234101.
50. Medford, A. J.; Vojvodic, A.; Hummelshøj, J. S.; Voss, J.; Abild-Pedersen, F.; Studt, F.; Bligaard, T.; Nilsson, A.; Nørskov, J. K., From the Sabatier principle to a predictive theory of transition-metal heterogeneous catalysis. *Journal of Catalysis* **2015,** *328*, 36-42.
51. Lum, Y.; Cheng, T.; Goddard, W. A., III; Ager, J. W., Electrochemical CO Reduction Builds Solvent Water into Oxygenate Products. *Journal of the American Chemical Society* **2018,** *140* (30), 9337-9340.
52. He, T.; Reuter, K.; Du, A., Atomically dispersed asymmetric Cu–B pair on 2D carbon nitride synergistically boosts the conversion of CO into C2 products. *Journal of Materials Chemistry A* **2020,** *8* (2), 599-606.
53. Peng, H.-J.; Tang, M. T.; Halldin Stenlid, J.; Liu, X.; Abild-Pedersen, F., Trends in oxygenate/hydrocarbon selectivity for electrochemical CO(2) reduction to C2 products. *Nature Communications* **2022,** *13* (1), 1399.
54. Mao, X.; Gong, W.; Fu, Y.; Li, J.; Wang, X.; O'Mullane, A. P.; Xiong, Y.; Du, A., Computational Design and Experimental Validation of Enzyme Mimicking Cu-Based Metal–Organic Frameworks for the Reduction of CO2 into C2 Products: C–C Coupling Promoted by Ligand Modulation and the Optimal Cu–Cu Distance. *Journal of the American Chemical Society* **2023,** *145* (39), 21442-21453.
55. Chen, Z.; Zhao, J.; Zhao, J.; Chen, Z.; Yin, L., Frustrated Lewis pairs photocatalyst for visible light-driven reduction of CO to multi-carbon chemicals. *Nanoscale* **2019,** *11* (43), 20777-20784.